

Small-angle X-ray microdiffraction from fibrils embedded in tissue thin sections

 Prakash Nepal,^a Abdullah Al Bashit,^b Lin Yang^c and Lee Makowski^{a,d,*}

^aDepartment of Bioengineering, Northeastern University, Boston, MA, USA, ^bDepartment of Electrical and Computer Engineering, Northeastern University, Boston, MA, USA, ^cNational Synchrotron Light Source II, Brookhaven National Laboratory, Upton, NY, USA, and ^dDepartment of Chemistry and Chemical Biology, Northeastern University, Boston, MA, USA. *Correspondence e-mail: l.makowski@northeastern.edu

Received 8 May 2022

Accepted 11 October 2022

Edited by V. T. Forsyth, Lund University, Sweden, and Keele University, United Kingdom

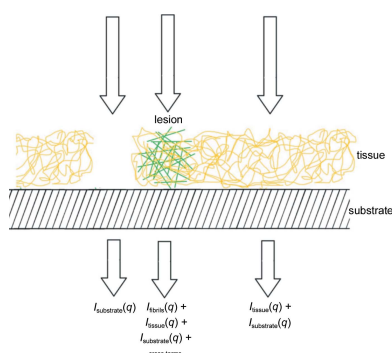
Keywords: small-angle X-ray scattering; SAXS; scanning microdiffraction; amyloids; Alzheimer's disease.

Supporting information: this article has supporting information at journals.iucr.org/j

Small-angle X-ray scattering (SAXS) from fibrils embedded in a fixed, thin section of tissue includes contributions from the fibrils, the polymeric matrix surrounding the fibrils, other constituents of the tissue, and cross-terms due to the spatial correlation between fibrils and neighboring molecules. This complex mixture severely limits the amount of information that can be extracted from scattering studies. However, availability of micro- and nano-beams has made the measurement of scattering from very small volumes possible, which, in some cases, may be dominated by a single fibrillar constituent. In such cases, information about the predominant species may be accessible. Nevertheless, even in these cases, the correlations between the positions of fibrils and other constituents have a significant impact on the observed scattering. Here, strategies are proposed to extract partial information about fibril structure and tissue organization on the basis of SAXS from samples of this type. It is shown that the spatial correlation function of the fibril in the direction perpendicular to the fibril axis can be computed and contains information about the predominant fibril structure and the organization of the surrounding tissue matrix. This has significant advantages over approaches based on techniques developed for X-ray solution scattering. Examples of correlation calculations in different types of samples are given to demonstrate the information that can be obtained from these measurements.

1. Introduction

Understanding the molecular basis of developmental or disease processes may require detailed information about the distribution of constituents throughout a tissue. For instance, immuno-histochemistry can be used to map the distribution of specific epitopes within tissues. However, methods based on optical microscopy often have inadequate resolution for the questions being asked, and techniques that probe the molecular structure of constituents more deeply are required. X-ray scattering from thin sections of tissue is rarely attempted because the heterogeneous mixture of constituents makes data interpretation difficult, the disruption of native structure intrinsic to sample preparation may destroy relevant structural features, and the disorientation and disorder of structures that do survive weaken and obscure the data collected. However, the availability of micro- and nano-beams can facilitate the measurement of scattering from very small volumes which, in some cases, may be populated largely by a single constituent. Furthermore, some classes of relevant structures, including pathological fibrillar protein deposits implicated in Alzheimer's and other neurodegenerative diseases, have robust architectures that are particularly resilient to the physical and chemical insults of sample



OPEN ACCESS

Published under a CC BY 4.0 licence

preparation. The aim of formaldehyde fixation and ethanol dehydration is to create a rigid, cross-linked polymer matrix. There have been extensive studies on the chemistry of formaldehyde reactions with amino acids and proteins (French & Edsall, 1945; Werner *et al.*, 2000), the impact on availability of epitopes for immunostaining (Werner *et al.*, 2000) and its effect on FTIR spectra (Zohdi *et al.*, 2015). These studies have shown that fixation preserves most protein secondary structures (Zohdi *et al.*, 2015) and epitopes (Werner *et al.*, 2000). Neuropathological fibrils stabilized by a cross- β core structure appear to be highly resilient to these treatments and are left intact, trapped within the cross-linked matrix (Liu *et al.*, 2016). Of particular importance to the analysis of small-angle X-ray scattering (SAXS) data, ethanol dehydration alters the electron density contrast between scattering particles and their surroundings and removes essentially all lipids (Zohdi *et al.*, 2015).

In many cases the fibrillar structures of interest are ‘frozen’ with random orientation in the matrix of fixed tissue and scattering from these fibrils might be considered analogous to solution scattering of fibrils in aqueous solution. However, the presence of a cross-linked macromolecular network in which the fibers are embedded presents significant challenges for analysis of scattering data. In this paper, we present an analysis of the properties of scattering from fibrillar objects embedded within a polymeric matrix and provide strategies for extracting information from these data. The methods described are of particular relevance to analysis of pathological protein deposits in human brain tissue.

SAXS is routinely used to obtain the shape and size of globular molecules in solution (Glatter & Kratky, 1982; Svergun & Stuhmann, 1991; Svergun & Koch, 2003; Koch *et al.*, 2003; Pollack, 2011; Putnam *et al.*, 2007; Lattman *et al.*, 2018). But conventional methods for analysis of SAXS data are not well suited to dealing with fibrils that have very long axial ratios, or scattering particles embedded in a polymeric matrix. SAXS data are frequently used to calculate the pair distribution function (PDF) (Svergun, 1992; Liu & Zwart, 2012; Hong & Hao, 2009): an r^2 -weighted histogram of the interatomic vector lengths in a scattering particle. However, the PDF is less informative when the scattering particle is a fibril of indeterminate length in which case the maximum interatomic vector length routinely estimated from the PDF is not well defined. In these cases, use of cross-section scattering functions is preferred (Porod, 1948; Kratky & Porod, 1948; Guinier & Fournet, 1955; Kratky, 1963; Glatter, 1980; Langkilde *et al.*, 2015). Here we demonstrate the utility of this approach, which is possible when equatorial scattering can be isolated from off-equatorial scattering. In particular, when the axial repeat distance of a fibril is less than ~ 30 Å, small-angle intensity may be attributed entirely to equatorial scattering (as defined by conventional fiber diffraction methods) and the equatorial intensity can be derived from the observed intensity by a simple geometric correction (Makowski, 1978). The resulting equatorial intensity can be used to calculate a ‘cross-section PDF’ (Glatter, 1980), analogous to the conventional PDF, but representing a histogram of the interatomic distances

projected onto the equatorial plane of the fibril. The length of the scattering fibril is irrelevant for this calculation.

A second change from conventional SAXS analysis is a focus on the correlation function (rather than the PDF). This has the advantage that the correlation function is much less sensitive to errors in measurement of intensity at very small scattering angles or the absence of intensity measurements very near zero angle. The lack of sensitivity of errors at low q is due to the fact that intensity is multiplied by q in order to obtain the correlation function. This suppresses the impact of errors at low q . The correlation function is the probability that, given there is an atom at some origin position, there is also one at a distance r . As is the case for the PDF, the correlation function can be defined for conventional (spherical) SAXS analysis or for the fibrous (cross-sectional) case where the relevant distances are those perpendicular to the fiber axis.

Here, we start with an overview of sample preparation and fiber diffraction theory and then present examples of scattering from fibrils in environments of increasing complexity. Starting with calculation of scattering from solid cylinders, we progress to scattering from molecular models of fibrils, analysis of scattering from fibrils in aqueous solution and concentrated gels, and finally to fibrils embedded in tissue. This progression allows us to demonstrate the impact of the milieu in which the structures are immersed on the properties observed.

2. Methods

2.1. Sample preparation

Data from tissue samples described here were collected from samples prepared at the Massachusetts Alzheimer’s Disease Research Center (MADRC) at the Massachusetts General Hospital using standard neuropathological processes to produce 20 μm sections with chemical and physical properties typical of histological sections as previously described (Liu *et al.*, 2016). The sample described in this manuscript was from an Alzheimer’s disease case. These unstained sections are thicker than conventional histological sections in order to increase the volume of material irradiated. A 5 μm beam was scanned over a rectangular region of interest (ROI) chosen on the basis of examination of serial sections stained for amyloid beta ($A\beta$) and tau proteins. Regions exhibiting high levels of $A\beta$ or tau were chosen for examination. Tissue sections were spread on either $1 \times 1 \text{ cm}^2$ mica films (12 μm thick) or $2.7 \times 2.7 \text{ mm}^2$ SiN membranes (1 μm thick) and then mounted on sample holders printed to LiX specifications (see below). The sample holders were mounted directly on the LiX beamline stage (Yang *et al.*, 2020, 2022) in air, but in a geometry to minimize the air gap (Yang *et al.*, 2022).

2.2. Data collection

Data collection was carried out at the LiX beamline at the NSLS-II synchrotron source at Brookhaven National Laboratory. Tissue sections mounted on mica or SiN films were scanned with a 5 μm X-ray microbeam using 5 μm steps

to collect diffraction patterns as a function of position on a square grid across the tissue section. Scans were carried out over a rectangular area of between $300 \times 300 \mu\text{m}^2$ (3600 diffraction patterns) and $600 \times 600 \mu\text{m}^2$ (14 400 diffraction patterns). An exposure time of 0.5 s was used and (including data transfer and sample step) approximately 0.8 s was required per exposure, or about 48 min for a $300 \times 300 \mu\text{m}^2$ ROI. Data were collected on SAXS and wide-angle X-ray scattering (WAXS) detectors simultaneously (see Fig. 1), and were circularly averaged and merged using LiX-specific software. Radiation damage was assessed by multiple scans of selected tissue regions to ensure that scattering from fibrils was not altered by X-ray exposure.

Data from *in vitro* assembled A β fibrils and tobacco mosaic virus (TMV) particles in solution used in the calculations described here have been reported previously (Roig-Solvas & Makowski, 2017). Data from concentrated gels of TMV particles are from Caspar (1955).

2.3. Data processing

Intensities in diffraction patterns were pre-processed to remove scattering from the mica films used as substrates for the tissue. This involved the ‘masking’ of peaks due to mica using a modification of LiX-specific software (Yang *et al.*, 2020). Three of these peaks can be seen near the left and top edges of the diffraction pattern in Fig. 1(a). After masking, data from the WAXS and SAXS detectors [Figs. 1(a) and 1(b)] were circularly averaged, merged and scaled using LiX-specific software, resulting in intensity distributions such as those in Figs. 1(c) and 1(d). All intensities were corrected for small fluctuations in beam intensity as measured at the LiX beamline prior to further processing. The location of pathological protein deposits can usually be determined on the basis

of intensity observed at $q \approx 1.34 \text{ \AA}^{-1}$ (corresponding to a spacing of 4.7 Å). This intensity was calculated from circularly averaged data for all patterns in an ROI and displayed as a ‘heat map’ like the one in Fig. 1(e), showing the distribution of relative intensities at a spacing of 4.7 Å in data from 4941 (61×81) scattering patterns in a $300 \times 400 \mu\text{m}^2$ ROI.

Correlation functions were calculated using an indirect Fourier transform (Glatter, 1980) with some modifications. The indirect Fourier transform as utilized by Glatter (1980) and Svergun (1992) requires an initial estimate of the maximum length of interatomic vectors in a scattering particle. In scattering from very long fibrils, that maximum length provides little constraint on the calculation. Although Glatter (2018) hints that some cross-sectional information can be derived from the ‘spherical’ pair correlation function, $P_s(r)$, it is important to distinguish between the $P_s(r)$, calculated with spherical geometry and the cross-sectional pair-correlation function $P_c(r)$, calculated using cylindrical geometry. Furthermore, when embedded in a tissue matrix, very long interatomic correlations may be present. In many cases those correlations may give rise to scattering at angles that are sufficiently small to preclude their measurement. In such cases, the maximum correlation distance observable is dictated by q_{min} . The maximum interatomic vector length used in the indirect transform is then chosen to be $(2\pi/q_{\text{min}})$ rather than d_{max} . This results in the calculation of correlation functions that represent a lower bound on correlations within and among particles in the scattering volume.

2.4. Background subtraction

Lesions commonly found in brain tissue in Alzheimer’s disease contain high concentrations of fibrillar structures made up of either A β peptides that are the primary constituents of

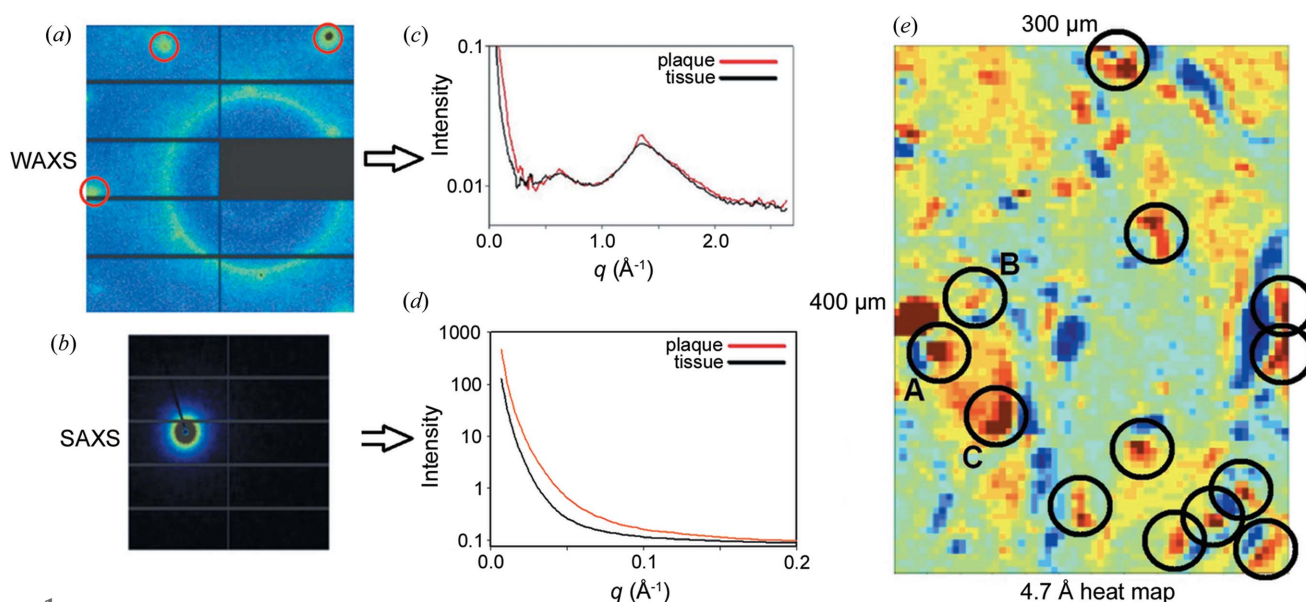


Figure 1 X-ray data from a histological thin section of brain tissue. Scattering data are collected simultaneously on (a) WAXS and (b) SAXS detectors. Red circles in (a) indicate the locations of peaks due to the mica substrate. Scattering from the mica substrate is subtracted and the resulting intensities are circularly averaged and merged in (c) and (d). The scattering at 4.7 Å spacing is typical of cross- β structures, including those made from A β or tau. (e) Maps of intensity at 4.7 Å spacing as measured in 4941 scattering patterns in a ROI make it possible to locate lesions (circles).

‘plaques’ (Cohen *et al.*, 2015; Qiang *et al.*, 2017) or tau proteins that are the predominant constituents of ‘neurofibrillary tangles’. Other tissue constituents permeate the lesions, surround the fibrils and contribute to the observed scattering. Usually, the overall intensity distribution in scattering from lesions is very similar to that observed from tissue adjacent to the lesions. But it is distinguished by the presence of a sharp peak at 4.7 Å spacing arising from the cross-β spine of the fibrils. Although the diffuse scattering from a lesion is similar in overall shape to that from adjacent tissue, it is usually somewhat more intense. This increased intensity appears to be caused by a greater density of material within the lesion compared with adjacent tissue (Nepal & Saldin, 2018). Scattering from the non-fibrillar tissue constituents is removed from fibrillar scattering within the plaque by assuming that the scattering of the tissue constituents within the lesion is the same as that in a neighboring region devoid of fibrils. Five background patterns are selected from regions adjacent to potential lesions and averaged. Since scattering from the underlying mica substrate does not require scaling, we carried out subtraction according to $I = (I_l - I_b) - a(I_t - I_b)$, where I_l is the observed scattering from the lesion, I_t is that observed from proximal tissue and I_b is the background observed from scattering of mica devoid of tissue (Bashit *et al.*, 2022). In our experience I_b is relatively invariant over the millimetre length scales of individual mica films, but may vary over centimetre length scales. The scale factor a is chosen to minimize the difference between plaque and background intensities in the range $1.6 < q < 2.0 \text{ \AA}^{-1}$, where all evidence has indicated the fibrillar scattering is weak.

2.5. Scattering from tissue

A thin section of fixed human brain tissue contains a network of cross-linked macromolecules, largely dehydrated and adhered to a solid substrate. In tissue from Alzheimer’s subjects these sections contain occasional lesions (plaques or tangles) in which pathological fibrillar structures may be the predominant constituent (Fig. 2). When the constituents exhibit essentially no orientation, the (circularly symmetric) scattering from these samples is given by the Debye formula

$$I(q) = \sum_{i,j} f_i f_j \frac{\sin(r_{ij}q)}{r_{ij}q}, \quad (1)$$

where the sum is over all atoms in the scattering volume, r_{ij} is the distance between atoms i and j , f_i is the scattering factor of atom i and q is the momentum transfer [$q = 4\pi \sin(\theta)/\lambda$, where 2θ is the scattering angle and λ is the wavelength of the incident X-rays]. In scattering from the lesions embedded within the tissue sample, there will be contributions from fibrils, other tissue constituents and the support substrate (mica film):

$$I_{\text{lesion}}(q) = \sum_{\text{fibrils}} f_{fi} f_{fj} \frac{\sin(r_{fi}q)}{r_{fi}q} + \sum_{\text{tissue}} f_{ti} f_{tj} \frac{\sin(r_{ti}q)}{r_{ti}q} + \sum_{\text{cross-terms}} f_{fi} f_{tj} \frac{\sin(r_{fi}q)}{r_{fi}q} + I_{\text{substrate}}(q), \quad (2)$$

where f_{fi} represents the scattering factor of atoms within the fibrils, f_{ti} that of atoms within the tissue and $I_{\text{substrate}}(q)$ the background from the mica substrate. The physical separation between substrate and lesion or tissue means that cross-terms with the substrate correspond to interatomic vectors of lengths that will not measurably contribute to the observed scattering. If the structure of the tissue network within the lesion is essentially identical to that outside the lesion, the second and fourth terms on the right side of equation (2) can be removed by subtracting intensity observed from a lesion-free region of the tissue. However, the cross-terms between fibrils and tissue are not removed by this subtraction. If the molecular environment within the tissue is completely unstructured, as is the case outside the hydration shell of macromolecules in aqueous solution, the cross-terms would contribute relatively little to the scattering (Park *et al.*, 2009) and could be, to a large extent, ignored. However, this is not the case for fixed tissue. Therefore, we can calculate directly from observations:

$$I_{\text{lesion}}(q) - I_{\text{tissue}}(q) - I_{\text{substrate}}(q) = \sum_{\text{fibrils}} f_{fi} f_{fj} \frac{\sin(r_{fi}q)}{r_{fi}q} + \sum_{\text{cross-terms}} f_{fi} f_{tj} \frac{\sin(r_{fi}q)}{r_{fi}q}. \quad (3)$$

The first term on the right-hand side of equation (3) contains information about the structure of individual fibrils and the second term information about the correlation in the positions of tissue constituents with the fibrils. A partial separation of the contribution of these two terms may be possible since the first term is dominated by short interatomic vectors and the second term by longer vectors.

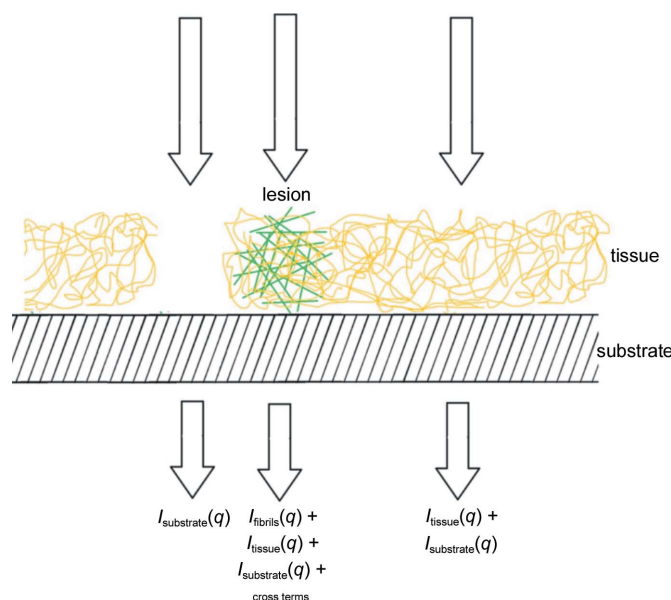


Figure 2 Diagram of tissue sample mounted on a solid substrate and attribution of the measured scattering intensity to the components of the system that can be collected.

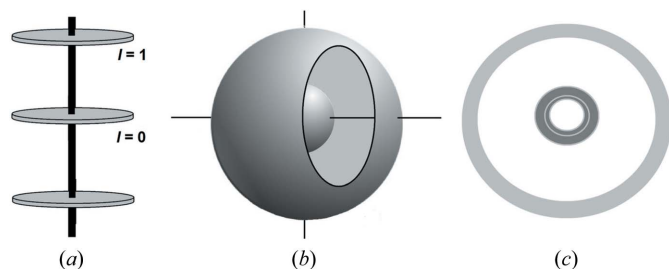


Figure 3
 (a) Diffraction from a periodic, fibrous structure is limited to layer planes spaced at distances reciprocal to the axial repeat of the fiber. The equator is indexed as $l = 0$, the first layer line as $l = 1$ and so on. For a cross- β structure the axial repeat is ~ 4.7 Å. When the fibrous structures are completely disoriented, the fiber pattern is spherically averaged in reciprocal space (b), giving rise to a diffraction pattern that is circularly symmetric (c). The disorientation spreads the two-dimensional layer planes (including the equator) onto three-dimensional surfaces.

2.6. Fiber diffraction

Fibrous biological assemblies are usually helical arrangements of identical subunits, the Fourier transform of which is a series of layer planes perpendicular to the fiber axis, arranged at spacings reciprocal to the axial repeat of the fiber (Fig. 3). Cross- β structures such as amyloid fibrils are composed of stacked A β peptides with an axial spacing of ~ 4.7 Å, and the intensity in the corresponding diffraction patterns is limited to layer planes spaced at $1/4.7$ Å⁻¹, the first order of which is frequently observed in diffraction patterns from these structures (Fig. 1). In tissue these fibrils exhibit little or no preferred orientation and give rise to scattering patterns that are circularly symmetric, or nearly so, as shown in Fig. 3. These patterns can be divided into the intensity at q values smaller than $1/4.7$ Å⁻¹, which is due to the intensity in the equatorial plane of the fiber pattern, and the intensity at $q > 1/4.7$ Å⁻¹, which will be dominated by scattering from the first layer plane. Analysis of the equatorial scattering can provide information about the diameter and shape of the fibrils and the arrangement of material around the fibril within the tissue (Roig-Solvas & Makowski, 2017). Comparison of the shape of the 4.7 Å reflection with that predicted from high-resolution structures obtained by cryoEM studies of isolated or *in vitro*-assembled material may provide identification of the precise structure within the scattering volume (Bashit *et al.*, 2022). In this report, we limit our analysis to the small-angle regime.

3. Results

3.1. Calculation of scattering from disoriented solid cylinders

Interpretation of the small-angle scattering from disoriented fibrils requires consideration of the impact of disorientation of the fibrils, the finite and often heterogeneous and indeterminate length of the fibrils, and the impact of components of the surrounding tissue on scattering from the fibrils. At sufficiently low resolution, fibrils are roughly solid cylindrical structures. The Fourier transform of a solid cylinder of radius r_{cyl} and length h is (Oster & Riley, 1952)

$$F(q_x, Z) = \frac{J_1(q_x r_{\text{cyl}})}{q_x r_{\text{cyl}}} \frac{\sin(hZ/2)}{hZ/2}, \quad (4)$$

where q_x is the distance from the cylindrical axis in reciprocal space, Z is the distance from the equator, $J_1(x)$ is the Bessel function of the first kind $J_n(x)$ with $n = 1$. For infinitely long cylinders the three-dimensional Fourier transform is confined to the equator ($Z = 0$) and equation (4) reduces to that for Fraunhofer diffraction by a circular aperture first derived by Airy (1835). Scattering from randomly oriented solid cylinders exhibiting no correlation of spatial positions can be readily computed from equation (4). That intensity can be used to calculate the PDF, $P_s(r)$ (Svergun & Koch, 2003), according to

$$P_s(r) = \frac{1}{2\pi^2} r^2 \int_0^\infty I(q) \frac{\sin(qr)}{qr} q^2 dq, \quad (5)$$

where q is the distance from the origin and $P_s(r)$ is an r^2 -weighted histogram of the lengths of interatomic vectors within the scattering object as conventionally calculated from SAXS data from globular proteins for all possible pairs of points (within the scattering particle). The subscript 's' is introduced here to distinguish it from the cross-section PDF defined in the next paragraph. The correlation function, $a_s(r)$ is related to $P_s(r)$ by

$$a_s(r) = P_s(r)/r^2. \quad (6)$$

In the analysis of scattering from tissues the correlation function has advantages over the PDF because it damps the impact of long-range interatomic vectors that are attributed to either the length of the fibril or the spatial correlations between the fibrils of interest and the surrounding polymeric matrix. Although these terms may provide information about tissue structure within the lesions, they are prone to high uncertainty and are very sensitive to the smallest q for which intensities can be accurately measured. In scattering from a sample of randomly oriented fibrils with sufficiently short axial repeat, it is possible to recover the equatorial intensity from the observed intensity through multiplication by a geometric correction factor that, except for very small q values, is approximately equal to q (Makowski, 1978). For helical assemblies with longer axial repeat (say $\gtrsim 30$ Å), disorientation may lead to a mixing of equatorial and off-equatorial scattering, precluding accurate measurement of intensities on the equator. Equatorial scattering can be analyzed in a manner analogous to spherically averaged data, resulting in a 'cross-section PDF', $P_c(r)$, that is a histogram of the lengths of interatomic vectors 'projected onto a plane perpendicular to the fiber axis' (Roig-Solvas & Makowski, 2017):

$$P_c(r) = 2\pi r \int_0^\infty I_e(q) J_0(qr) q dq, \quad (7)$$

where $I_e(q)$ is the equatorial scattering ($l = 0$ plane), J_0 is the zeroth-order Bessel function and $P_c(r)$ is the cross-section PDF. Analogously to the spherical case, a cross-section correlation function, $a_c(r)$, can be calculated from the cross-section PDF (Glatter, 1980) by

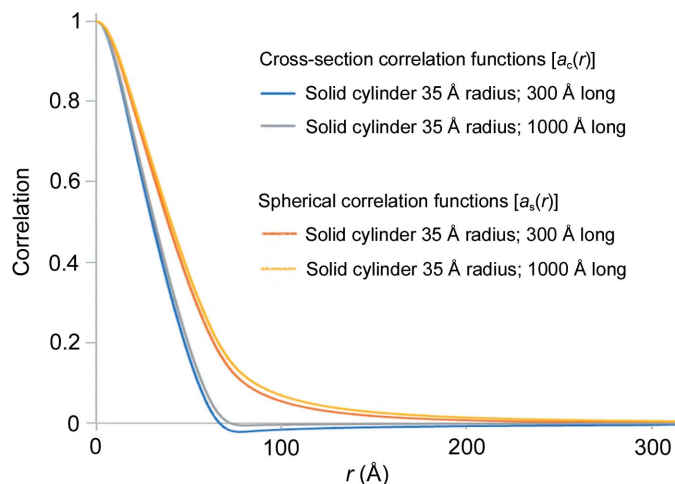


Figure 4 Spherical and cross-sectional correlation functions for solid cylinders 35 Å in radius and 300 or 1000 Å in length calculated from computationally generated scattering intensities. The cross-section correlation functions approach zero at the diameter (70 Å). Spherical correlation functions extend out to a distance equal to their length although for long cylinders its value is quite low for r much greater than the diameter of the cylinder. The slight difference between the cross-section correlation functions calculated for the cylinders 300 and 1000 Å in length is due to approximations required to estimate equatorial scattering at very small q .

$$a_c(r) = P_c(r)/r. \quad (8)$$

The relationships between these functions are depicted in Fig. 4 for the case of solid cylinders of length 300 or 1000 Å and radius 35 Å. Correlation functions were obtained by an indirect Fourier transform (Glatter, 1980) of calculated isotropic SAXS intensities calculated for a solid cylinder of these dimensions and shown in Fig. S1 of the supporting information. Equations (5), (6), (7) and (8) were used for the calculation of correlation functions and related software is available from the authors on request. For the calculation of the cross-section correlation function, the equatorial intensity was approximated by multiplying the spherically averaged intensity by a geometric correction factor proportional to q . Fig. 4 demonstrates that these two correlation functions provide direct information on the size and shape of the scattering objects. The maximum vector length for $a_s(r)$ corresponds to the length of the cylinder; the maximum vector length for $a_c(r)$ corresponds to its diameter. These functions were computed with data extending to $q = 0.3 \text{ \AA}^{-1}$ so that they correspond to calculations from SAXS data. The limited resolution results in a small overshoot of zero correlation. As a further demonstration of the properties of these functions, the cross-section correlation function was calculated for a model amyloid fibril constructed from 30 layers of A β peptides with each layer having the structure of complete A β (1-42) (PDB entry 5oqv; Gremer *et al.*, 2017), separated by 4.7 Å from its nearest neighbors. Overall, this structure is $\sim 141 \text{ \AA}$ long and 56 Å in diameter. CRY SOL (Svergun *et al.*, 1995) was utilized to calculate the SAXS intensity for the model using default parameters. As can be seen from Fig. 5 the cross-section correlation function of 5oqv compares well with the correla-

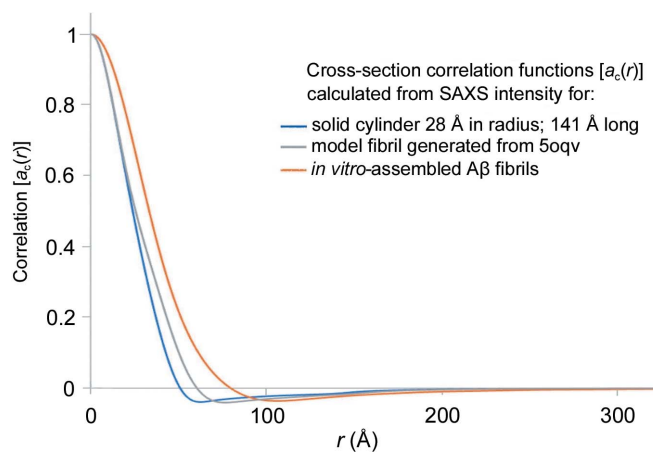


Figure 5 Comparison of cross-section correlation functions from a solid cylinder, from a model amyloid fibril generated from 5oqv and as calculated from SAXS data from *in vitro*-assembled A β fibrils. At low r , the correlation function of the solid cylinder and the PDB model are indistinguishable since the overall dimensions of the fibril and cylinder are essentially the same. They deviate at larger r due to variation from cylindrical shape at the outer surface of the model fibril. Comparison suggests that the *in vitro*-assembled fibrils are significantly larger than the model fibril, consistent with previous modeling of the fibril structure (Roig-Solvas & Makowski, 2017).

tion function of a 28 Å radius solid cylinder at low r , but deviates at higher r due to the non-cylindrical shape of the model amyloid fibril.

3.2. Correlation function of A β fibrils in aqueous solution

Next, we consider correlation functions calculated from experimental scattering intensities collected from amyloid fibrils in aqueous solution. This is a far simpler environment for scattering than a fixed tissue and it is instructive to consider the scattering in solution as a baseline (Svergun & Koch, 2002; Svergun & Koch, 2003) for understanding the observations from scattering when the fibrils are in more complex environments.

We reported SAXS from *in vitro*-assembled A β peptides (Roig-Solvas & Makowski, 2017) and have used those data here to compute cross-section correlation functions. As shown in Fig. 5, the correlation function calculated from the SAXS data displays properties expected of a fibril with a cross-section radius greater than that of the model fibril constructed from PDB entry 5oqv. We have previously shown that the fibrils in this sample have multiple protofibrils, resulting in an average cross section greater than that of fibril 5oqv and similar to *in vitro*-assembled fibrils observed by cryoEM (Meinhardt *et al.*, 2009). The results in Fig. 5 are consistent with these observations.

3.3. Correlation functions of solutions and concentrated gels of TMV

SAXS data from increasingly concentrated solutions exhibit features resulting from interparticle interference and that interference can be characterized through the cross-sectional correlation function. As an example of this, we consider

scattering from dilute solutions (Costa *et al.*, 2016) and concentrated gels (Caspar, 1955) of tobacco mosaic virus. TMV particles are cylindrical rods about 3000 Å long and 180 Å in diameter. Cross-section and spherical correlation functions were calculated from solution scattering data of disoriented dilute solutions provided by Martha Brennich (ESRF) and equatorial scattering from concentrated gels extracted from the thesis of Dr Donald Caspar (1955) (shown in Fig. S2). Fig. 6 displays the results of these calculations.

TMV in concentrated gels is highly oriented, making accurate measurement of equatorial scattering and observation of dramatic interparticle interference effects possible (Caspar, 1955). The particles in these gels form a partially ordered liquid-like two-dimensional packing with nearest-neighbor distances averaging about 275 Å. This is reflected in the peak in the cross-section correlation function in Fig. 6. This correlation function also exhibits a minimum at about 150 Å, at which point the correlation function is considerably below zero. Negative values for correlation functions are due to regions of electron density below the average electron density of the scattering volume. In these gels, particles exhibit some repulsion, making close packing unlikely and resulting in an electron density immediately outside each particle that is below the average for the sample. In the calculation of correlation functions this generates the possibility of a negative correlation at the corresponding distance. This negative correlation is also responsible for the cross-section correlation function crossing zero at $r \approx 100$ Å, well below the diameter of the particle, demonstrating that interparticle interference effects can impact estimates of the radius of scattering particles using the cross-section correlation function. The cross-section correlation function calculated from solution scattering approaches zero at about 155 Å, which is somewhat smaller than expected for the 170–180 Å diameter particles, indicating that even in dilute solution some interparticle effects are present. The spherical correlation function calculated from a dilute solution of TMV approaches zero asymptotically beyond $r = 400$ Å, reflecting the impact of the particle

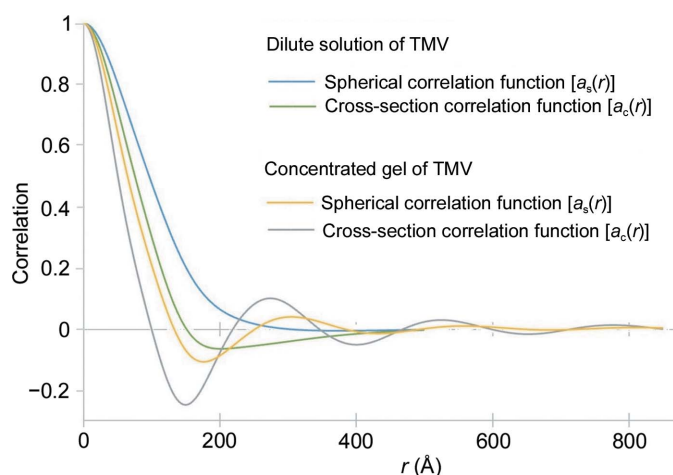


Figure 6 Correlation functions of TMV in dilute solution and concentrated gel.

length on the observed data. While the spherical correlation of the TMV particle should theoretically extend to 3000 Å, intensity measurements were limited to $q > 1/400 \text{ Å}^{-1}$ and intensity fluctuations caused by longer correlations were not observable as indicated in the *Methods* section.

3.4. Correlation function of A β fibrils embedded in fixed tissue

Fig. 7 includes the cross-section correlation functions calculated from SAXS data derived from five positions in a single dense A β plaque embedded in human brain tissue (corresponding to the data shown in Figs. 1 and S3). For comparison, the correlation functions of a model constructed from 5oqv and as calculated from SAXS scattering from *in vitro*-assembled A β fibrils suspended in aqueous solution are included in Fig. 5. At radii less than the diameter of the fibrils, the cross-section correlation function is dominated by interatomic vectors within the fibril. At intermediate radii, there are cross-term contributions, precluding an accurate estimate of fibril diameter. At radii larger than the diameter, cross-terms between fibril and tissue (and fibril and fibril) will dominate. As seen in Fig. 7 the correlation functions from different positions within the dense plaque are nearly indistinguishable at small r , suggesting that the predominant fibrils have the same diameter at each position. They are also nearly identical to the correlation function of the *in vitro*-assembled fibrils, but fall at larger radii than calculated from 5oqv. This strongly suggests that, *in situ*, these fibrils are composed of multiple protofilaments coalesced side-to-side to form larger-diameter fibrils. At $r \gg 30$ Å, the correlation function of fibrils within the plaque diverges from the correlation function of the isolated fibrils due to the cross-terms arising from the tissue matrix. The correlation at $200 \text{ Å} < r < 300 \text{ Å}$ varies by 5–10% at different positions in the plaque, suggesting that the mass density varies across the plaque. The correlations within the

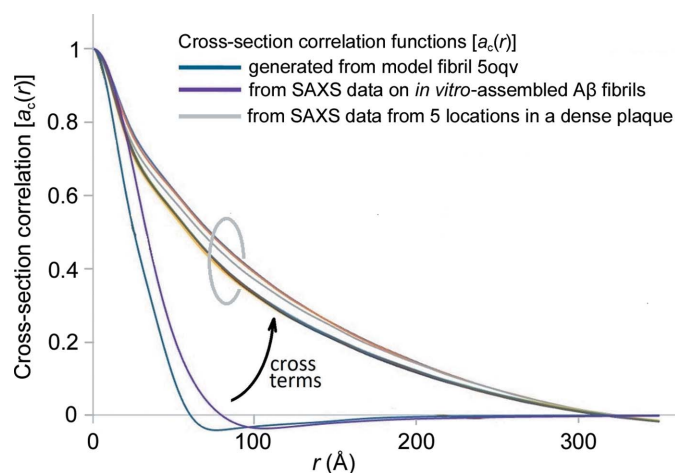


Figure 7 Cross-section correlation functions calculated for five different positions in the dense amyloid plaque denoted 'A' in the heat map in Fig. 1(e). Comparison of correlation functions calculated from SAXS data from *in vitro*-assembled fibrils and from computationally generated intensities from a fibril constructed using 5oqv.

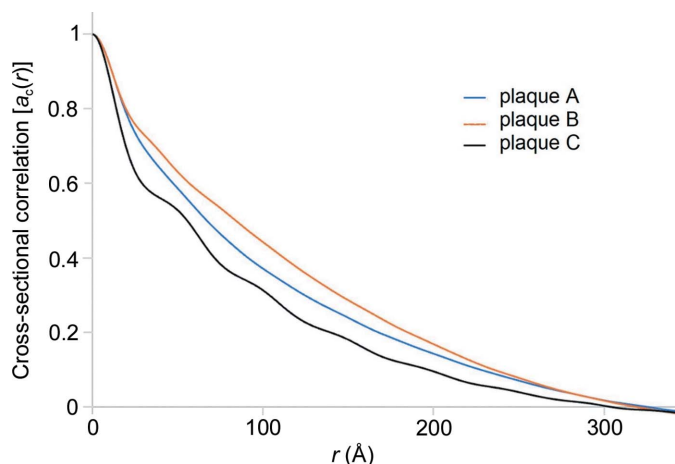


Figure 8
Cross-section correlation functions for three lesions in the tissue section in Fig. 1. Two plaques (A and B) appear to be very similar at low r , suggesting a similar if not identical fibrillar structure. The third exhibits a low- r regime with a shape that suggests the predominant scattering particle has smaller characteristic dimensions.

tissue section may extend to radii larger than that apparent in Fig. 7, but our ability to estimate their magnitude is limited by the minimum scattering angle for which accurate intensities can be measured. Estimation of correlation functions at $r \gtrsim 300$ Å is precluded by the X-ray camera geometry used.

In Fig. 8 the correlation functions of three plaques from the same tissue section are compared, as calculated from the data in Fig. S4. Two of those functions are nearly identical at low r , suggesting they are dominated by fibrils of identical or similar diameters (by comparing the red and blue curves at $r < 30$ Å). The other appears to have a smaller characteristic length (sharper correlation function at low r) and exhibits an oscillation in the correlation with a periodicity of ~ 50 Å. Analysis of the WAXS data from this lesion suggests it may correspond to a lipidic inclusion or a different non-cross- β type structure.

4. Discussion

Scattering from fibrillar structures in solution or embedded in a cross-linked matrix results in data that require special considerations in order to extract useful structural information. In aqueous solution, the scattering from fibrils can be predicted using conventional estimates based on atomic coordinates (Svergun *et al.*, 1995; Park *et al.*, 2009), but their length results in scattering features at very small scattering angles that may be difficult to measure or interpret. When the fibrils are embedded in a solid matrix, the situation is more complex: spatial correlations between the fibrils and the constituents of the polymer matrix surrounding them will have a significant impact on very small angle scattering. Furthermore, dehydration during sample preparation may increase electron density contrast between the fibrils and their surroundings, thereby enhancing the intensity of small-angle scattering relative to wide-angle scattering. Depending on the density of the matrix the electron density contrast between

fibril and surrounding tissue could be greater in a dehydrated tissue than in dilute aqueous solution, although that is not assured.

In this paper, we described the impact of correlations between fibrils and the other constituents in their immediate vicinity in terms of ‘cross-terms’ in equation (3). An alternative description of these correlations can be made by treating the fibril embedded in tissue as analogous to a protein in aqueous solution. Proteins in aqueous solution are surrounded by a hydration layer in which the water molecules take on a structure distinct from bulk water. To accurately predict SAXS data from the atomic coordinates of these proteins, the correlation between protein atoms and atoms in the hydration layer must be taken into account (Park *et al.*, 2009). This is the strategy we have taken in the formulations described here. However, an alternative formulation is possible in which the hydrated protein is defined to include all protein atoms and all water atoms within the hydration layer. If the hydration layer is chosen to be large enough that its outer layer is indistinguishable from bulk water, then there will be essentially no correlations between the positions of water atoms within and outside the hydration layer. Under such conditions, the ‘cross-terms’ will average to zero. By analogy, an ‘aggregated fibril’ within a tissue matrix might be defined to include both the fibril and the immediately adjacent tissue constituents that take on a distinct organization due to the presence of the fibril (for instance, by binding to or aggregating with the fibril). The advantage of this formulation is that it makes clear that the cross-section correlation function calculated from SAXS of fibrils in tissue describes the properties of the ‘aggregated fibrils’ within the scattering volume. For instance, the ~ 300 Å radial extent of the cross-section correlation functions plotted in Fig. 7 for an amyloid plaque would indicate that the presence of A β fibrils in this plaque impacts the organization of the fixed tissue out to a radius of at least ~ 150 Å from the fibril axis. The magnitude of correlation at radii greater than the radius of the fibril should provide an estimate for the degree of compaction of material in the immediate vicinity of the fibril (relative to that of bulk tissue). As demonstrated in Fig. 6, negative values of the correlation are possible if the density of tissue constituents in the immediate vicinity of the fibril is less than that of the bulk tissue.

It is common practice to calculate a PDF from SAXS data on globular proteins. This is because the domain structure and shape of globular proteins appear well represented in the PDF; and in dilute solutions there is little contribution from inter-protein correlations so there is a well defined r_{\max} beyond which the PDF is effectively zero. In scattering from fibrils, the conventional (whole-particle) SAXS PDF provides a less clear picture. First, r_{\max} is very large (roughly half the length of the fibril), making its estimate highly sensitive to the minimum q for which accurate intensities can be measured. Second, in scattering from fibrils of heterogeneous length, r_{\max} becomes ill defined. Third, r_{\max} is rigorously the maximum extent of spatial correlations in the sample. For fibrils embedded in a polymeric matrix, the spatial correlations

between fibril and surrounding matrix constituents may have very large correlation lengths, corresponding to very large r_{\max} , the estimation of which will be similarly sensitive to measurement errors in intensities at very small q . To address these challenges, we have utilized the cross-section correlation function (Glatter, 1980). This function is independent of the length of the fibrils and is less sensitive to intensity variation at very small q . It can be calculated for fibrils with axial repeats $\lesssim 30 \text{ \AA}$ for which equatorial intensities can be extracted from SAXS data (where we assume that SAXS data extend to $\sim 30 \text{ \AA}$ spacing). For fibrils with longer repeat distances, the mixing of equatorial and off-equatorial intensities due to disorientation will limit the maximum scattering angle to which equatorial scattering can be unambiguously measured.

The cross-section correlation function is readily calculated from the cross-section PDF which constitutes a histogram of interatomic distances ‘projected perpendicular to the fibril axis’. These cross-section functions are independent of fibril length and have proven useful for fibrils in solution (Roig-Solvas & Makowski, 2017). In scattering from fibrils embedded in fixed tissue, their form is impacted by the presence of other tissue constituents (as shown above). For these samples, the correlation function is preferred to the PDF since it is less sensitive to errors in intensity at small q , and to the minimum q for which intensities can be measured.

The spatial correlations between the fibril and the surrounding matrix will contribute to the cross-section correlation function calculated from the scattering of fibrils and may preclude an unambiguous estimate of the diameter of the fibrils themselves. The maximum extent of spatial correlations within the tissue matrix may be difficult to estimate since correlations that extend further than several hundred ångströms will give rise to scattering at very small angles that may not be accessible for some X-ray camera geometries. Nevertheless, the cross-section correlation function provides significant insight into the structure of the fibril–matrix mixture within the scattering volume.

It may be possible to estimate the density of the immediate microenvironment of a fibril from its cross-section correlation function. If that proves successful it will provide insight into the density and structural organization of the pathological lesions in which the fibrils are the predominant species. The way that the cross-section correlation function deviates from that expected from a uniform mass distribution may provide insight into the internal structure of a lesion. We have demonstrated that SAXS data collected from small scattering volumes of fixed tissue when dominated by pathological fibrillar aggregates can provide considerable insight into the structural organization of these lesions: $A\beta$ plaques or neurofibrillary tangles. Overall, the correlation functions introduced here lay out the properties of scattering from fibrillar objects embedded within a polymeric matrix, solution, gel *etc.* and offer unique approaches for extracting information from these data. The variation of these features may provide insights into the way these lesions assemble and grow during the progression of neurodegeneration (Murray *et al.*, 2011; Meisl *et al.*, 2021).

Acknowledgements

We would like to acknowledge the considerable contributions of Theresa R. Connors and Dr Bradley Hyman at the Massachusetts Alzheimer’s Disease Research Center (MADRC). All tissue samples were prepared by Theresa R. Connors at MADRC in collaboration with Dr Bradley Hyman.

Funding information

This work was supported in part by the National Institutes of Health (grant No. R21-AG068972). The Massachusetts Alzheimer’s Disease Research Center (MADRC) is supported by the National Institute on Aging (grant No. P30-AG-062421). The LiX beamline is part of the Center for BioMolecular Structure (CBMS), which is primarily supported by the National Institutes of Health (NIH), National Institute of General Medical Sciences (NIGMS) (grant No. P30GM133893), and by the DOE Office of Biological and Environmental Research (grant No. KP1605010). LiX also received additional support from the NIH (grant No. S10 OD012331). As part of NSLS-II, a national user facility at Brookhaven National Laboratory, work performed at the CBMS is supported in part by the US Department of Energy, Office of Science, Office of Basic Energy Sciences program (contract No. DE-SC0012704).

References

- Airy, G. B. (1835). *Trans. Camb. Philos. Soc.* **5**, 283.
- Bashit, A. A., Nepal, P., Connors, T., Oakley, D. H., Hyman, B. T., Yang, L. & Makowski, L. (2022). *Front. Neurosci.* **16**, 909542.
- Caspar, D. L. D. (1955). PhD thesis, Yale University, USA.
- Cohen, M. L., Kim, C., Haldiman, T., El Hag, M., Mehndiratta, P., Pichet, T., Lissemore, F., Shea, M., Cohen, Y., Chen, W., Blevins, J., Appleby, B. S., Surewicz, K., Surewicz, W. K., Sajatovic, M., Tatsuoka, C., Zhang, S., Mayo, P., Butkiewicz, M., Haines, J. L., Lerner, A. J. & Safar, J. G. (2015). *Brain*, **138**, 1009–1022.
- Costa, L., Andriatis, A., Brennich, M., Teulon, J.-M., Chen, S. W., Pellequer, J.-L. & Round, A. (2016). *BMC Struct. Biol.* **16**, 18.
- French, D. & Edsall, J. T. (1945). *Adv. Protein Chem.* **2**, 277–335.
- Glatter, O. (1980). *J. Appl. Cryst.* **13**, 577–584.
- Glatter, O. (2018). *Scattering Methods and Their Application in Colloid and Interface Science*. Amsterdam: Elsevier.
- Glatter, O. & Kratky, O. (1982). *Small Angle X-ray Scattering*. London: Academic Press.
- Gremer, L., Schölzel, D., Schenk, C., Reinartz, E., Labahn, J., Ravelli, R. B., Tusche, M., Lopez-Iglesias, C., Hoyer, W., Heise, H., Willbold, D. & Schröder, G. F. (2017). *Science*, **358**, 116–119.
- Guinier, A. & Fournet, G. (1955). *Small Angle Scattering of X-rays*. New York, London: John Wiley & Sons/Chapman and Hall.
- Hong, X. & Hao, Q. (2009). *Appl. Phys. Lett.* **94**, 083903.
- Koch, M. H. J., Vachette, P. & Svergun, D. I. (2003). *Q. Rev. Biophys.* **36**, 147–227.
- Kratky, O. (1963). *Prog. Biophys. Mol. Biol.* **13**, 105–173.
- Kratky, O. & Porod, G. (1948). *Acta Phys. Austriaca*, **2**, 133–147.
- Langkilde, A. E., Morris, K. L., Serpell, L. C., Svergun, D. I. & Vestergaard, B. (2015). *Acta Cryst.* **D71**, 882–895.
- Lattman, E. E., Grant, T. D. & Snell, E. H. (2018). *Biological Small Angle Scattering: Theory and Practice*. Oxford University Press.
- Liu, H. & Zwart, P. H. (2012). *J. Struct. Biol.* **180**, 226–234.

- Liu, J., Costantino, I., Venugopalan, N., Fischetti, R. F., Hyman, B. T., Frosch, M. P., Gomez-Isla, T. & Makowski, L. (2016). *Sci. Rep.* **6**, 33079.
- Makowski, L. (1978). *J. Appl. Cryst.* **11**, 273–283.
- Meinhardt, J., Sachse, C., Hortschansky, P., Grigorieff, N. & Fändrich, M. (2009). *J. Mol. Biol.* **386**, 869–877.
- Meisl, G., Hidari, E., Allinson, K., Rittman, T., DeVos, S. L., Sanchez, J. S., Xu, C. K., Duff, K. E., Johnson, K. A., Rowe, J. B., Hyman, B. T., Knowles, T. P. J. & Klenerman David (2021). *Sci. Adv.* **7**, eabh1448.
- Murray, M. E., Graff-Radford, N. R., Ross, O. A., Petersen, R. C., Duara, R. & Dickson, D. W. (2011). *Lancet Neurol.* **10**, 785–796.
- Nepal, P. & Saldin, D. K. (2018). *Phys. Rev. B*, **97**, 195426.
- Oster, G. & Riley, D. P. (1952). *Acta Cryst.* **5**, 272–276.
- Park, S., Bardhan, J. P., Roux, B. & Makowski, L. (2009). *J. Chem. Phys.* **130**, 134114.
- Pollack, L. (2011). *Annu. Rev. Biophys.* **40**, 225–242.
- Porod, G. (1948). *Acta Phys. Austriaca*, **2**, 255–292.
- Putnam, C. D., Hammel, M., Hura, G. L. & Tainer, J. A. (2007). *Q. Rev. Biophys.* **40**, 191–285.
- Qiang, W., Yau, W. M., Lu, J. X., Collinge, J. & Tycko, R. (2017). *Nature*, **541**, 217–221.
- Roig-Solvas, B. & Makowski, L. (2017). *J. Struct. Biol.* **200**, 248–257.
- Svergun, D. I. (1992). *J. Appl. Cryst.* **25**, 495–503.
- Svergun, D., Barberato, C. & Koch, M. H. J. (1995). *J. Appl. Cryst.* **28**, 768–773.
- Svergun, D. I. & Koch, M. H. (2002). *Curr. Opin. Struct. Biol.* **12**, 654–660.
- Svergun, D. I. & Koch, M. H. (2003). *Rep. Prog. Phys.* **66**, 1735–1782.
- Svergun, D. I. & Stuhrmann, H. B. (1991). *Acta Cryst.* **A47**, 736–744.
- Werner, M., Chott, A., Fabiano, A. & Battifora, H. (2000). *Am. J. Surg. Pathol.* **24**, 1016–1019.
- Yang, L., Antonelli, S., Chodankar, S., Byrnes, J., Lazo, E. & Qian, K. (2020). *J. Synchrotron Rad.* **27**, 804–812.
- Yang, L., Liu, J., Chodankar, S., Antonelli, S. & DiFabio, J. (2022). *J. Synchrotron Rad.* **29**, 540–548.
- Zohdi, V., Whelan, D. R., Wood, B. R., Pearson, J. T., Bambery, K. R. & Black, M. J. (2015). *PLoS One*, **10**, e0116491.